Laboratory Acousto-Mechanical Study Into Moisture-Induced Reduction of Fracture Stiffness in Granite

Rui Wu[1,2] , **Paul A. Selvadurai[3]** , **Ying Li[1,4]** , **Kerry Leith[1,5]** , **Qinghua Lei[1,6]** , and **Simon Loew[1]**

[1]Department of Earth Sciences, ETH Zürich, Zürich, Switzerland, [2]State Key Laboratory of Intelligent Coal Mining and Strata Control, China Coal Research Institute, Beijing, China, [3]Swiss Seismological Service, ETH Zürich, Zürich, Switzerland, [4]Department of Civil and Transportation Engineering, Hebei University of Technology, Tianjin, China, [5]Surface Geosciences, GNS Science, Lower Hutt, New Zealand, [6]Department of Earth Sciences, Uppsala University, Uppsala, Sweden

Abstract Water infiltration into fractures is ubiquitous in crustal rocks. However, little is known about how such a progressive wetting process affects fracture stiffness and seismic wave propagation, which are highly relevant for characterizing fracture systems in situ. We study the acousto-mechanical behavior of a free-standing fractured granite subjected to gradual water infiltration with a downward-moving wetting front over 12 days. We observe significant differences (i.e., by an order of magnitude) in wave amplitudes across the fractured granite compared to an intact granite, with both cases showing a strong correlation between wave amplitudes and wetting front movement. Effects of water infiltration into the fracture and surrounding matrix on seismic attenuation are captured by a numerical model with parameters constrained by experimental data. Back-calculated fracture stiffness decreases exponentially with the wetting front migration along the fracture. We propose that moisture-induced matrix expansion around the fracture increases asperity mismatch, leading to reduced fracture stiffness.

Plain Language Summary In the shallow layers of the Earth, hydrological cycles such as snowmelt, fog, dew, and rain have been shown to change the moisture content of crustal rocks, which can alter the elastic properties of natural fractures and affect the propagation of seismic waves. Understanding how seismic waves propagate in the near-surface environment is crucial for the assessment of earthquake hazards and the characterization of geologic heterogeneities. In this work, we perform well-controlled laboratory experiments to study the acousto-mechanical behavior of a single fracture in granitic rock subjected to progressive wetting over 12 days. We report that the fracture stiffness decreases exponentially as the wetting front advances along the fracture. Our research sheds light on an important question in fracture characterization: how elastic waves propagate across a fracture undergoing moisture-induced expansion.

1. Introduction

Fractures that are widely present in the Earth's crust often dominate the seismic, mechanical, and hydrogeological behavior of rock masses (Cook, 1992; Lei & Sornette, 2021a, 2021b; Pyrak-Nolte et al., 1990; Tsang & Witherspoon, 1981). Moisture content within rock masses can vary in response to the hydrological cycle that impacts the Earth's surface, through for example, evaporation, condensation, precipitation, snow/ice melt, and runoff. The moisture variations are also highly relevant to engineering activities, for example, groundwater extraction, slope stabilization, underground excavation, mine ventilation, and nuclear waste disposal. Moisture uptake/release could alter the mechanical properties of rock masses as reported by many case studies of natural hazards and engineering infrastructures. For example, slope stability related to ice/snow melting and/or rainfall (Burjánek et al., 2017), to seasonal humidity cycling-related mine failures (Chugh & Missavage, 1981), and fog-related tunnel wall spallation (Diederichs, 2007). The presence of moisture can lead to a decreased rock strength by reducing the specific surface energy (Baud et al., 2000). Thus, understanding the role of moisture on the mechanical behavior of rock masses is crucial for characterizing, modeling, and predicting many processes and phenomena in the Earth's surface and subsurface, which can be investigated using elastic waves that inherently carry information of the rock masses through which they traverse (Geimer et al., 2020; Weber et al., 2018).

Ultrasonic wave transmission is highly effective for detecting subtle mechanical changes of fractured rocks, supported by extensive experimental and analytical studies on contact mechanics (Cook, 1992; Gheibi & Hedayat, 2018; Kaproth & Marone, 2013; Kendall & Tabor, 1971; Nagata et al., 2008; Pyrak-Nolte et al., 1990;

Schoenberg, 1980; Scuderi et al., 2016; Shokouhi et al., 2020; Shreedharan et al., 2020, 2021; Tinti et al., 2016). Among these studies, fractures are modeled as non-welded interfaces consisting of contact patches and adjacent voids (Archard, 1957; Bowden & Tabor, 2001; Greenwood & Williamson, 1966; Johnson, 1985; Tsang & Witherspoon, 1981). Along interfaces, real contact area via distributed patches is small, for example, less than 10%, compared to the nominal contact area (Dieterich & Kilgore, 1994; Persson, 2006). As elastic waves travel through the real contact area, the displacement field is discontinuous, whereas the stress field remains continuous (Kendall & Tabor, 1971; Pyrak-Nolte et al., 1990; Schoenberg, 1980). The ratio of stress to displacement discontinuity defines fracture stiffness that controls the amount of transmitted wave energy. When the fracture is subjected to increased normal stress, the separation distance between the fracture walls decreases and the real contact area increases, leading to increased fracture stiffness. The real contact area, which is approximately proportional to the fracture stiffness, behaves akin to a "filter," allowing high-frequency wave contents to pass through the fracture (Pyrak-Nolte et al., 1990).

Laboratory investigations have focused on the mechanical response of fractured rocks, either dry or saturated, subjected to compression or shear, as examined through ultrasonic waves (Choi et al., 2014; Kame et al., 2014; Nagata et al., 2008; Pyrak-Nolte et al., 1990; Shreedharan et al., 2020). Little attention has been paid to fractured rocks undergoing progressive wetting due to spontaneous water imbibition which is important in nature. Previous studies (David, Barnes, et al., 2017; David, Sarout, et al., 2017; Wu, Selvadurai, Li, Sun, et al., 2023) revealed substantial variations in wave amplitudes as the wetting front progressively infiltrated an intact specimen. These elastic changes could be explained by the elastic wave refraction at the wetting front, which delineates the transition between the dry and wet regions (Knott, 1899; Kovalyshen, 2018; Zoeppritz, 1919). In this research, we further investigate water imbibition in a fractured specimen, aiming to understand the relationship between progressive wetting, wave transmission, and stiffness evolution.

2. Materials and Methods

2.1. Material Characterization

Tests are performed on Herrnholz granite which has been well characterized (Li et al., 2021, 2022; Wu, Selvadurai, Li, Sun, et al., 2023). Thin section analysis shows a granitic mineralogical assemblage of 50% quartz, 38% feldspar, and 11% mica. This granite is fine-grained with a mean crystal size of around 0.23 mm. Grain and bulk densities are 2.66 ± 0.0027 and 2.609 ± 0.001 g/cm^3, respectively. Water-accessible porosity is measured as $1.53\% \pm 0.007\%$ following a de-airing technique (A. P. S. Selvadurai et al., 2011). P-wave velocity structure reveals very weak (all below 2%) anisotropy, heterogeneity, and specimen variability. The P-wave velocity under oven-dried and water-saturated conditions is measured to be $4,538 \pm 13$ and $5,300 \pm 18$ m/s, respectively. Significant increases in P-wave velocity are attributed to wave-induced flow in microcracks (Müller et al., 2010; Wu, Selvadurai, Li, Sun, et al., 2023). Matrix permeability for water flow is extremely low, at approximately 7.4×10^{-19} m^2.

2.2. Specimen Preparation and Experimental Setup

In Figure 1a, we generate a semi-planar fracture in a notched beam subjected to a three-point bending test via a constant displacement rate of 1 μm/s. As the load approaches the peak strength (14.4 ± 0.5 kN) and subsequently exhibits a reduction greater than 5% of its peak strength, a servo-controlled failure detection will promptly relieve the load. This prevents the beam from being fully broken such that it is supported by rock bridges across the fracture. The fracture produced has an opening of about 0.05 mm near the notch, measured with a crack gauge, and is barely visible at its tip, about 16 mm from the bottom of the beam. A prismatic specimen (dimension: $65 \times 35 \times 90$ mm), containing part of the fracture, is extracted from the central part of the beam (Figure 1a).

We perform water imbibition tests on this extracted specimen placed in a free-standing state. The specimen is oven-dried at 80°C and then acclimated to ambient laboratory conditions for 16 hr. Subsequently, distilled water is introduced to the top surface of the specimen via a filter paper that is immersed in a water reservoir where the water table is maintained for 270 hr. Bond number, a dimensionless parameter comparing the gravitational to capillary forces (Su et al., 1999), is calculated to be below 2×10^{-3} for matrix (estimated from average pore size of below 100 nm) and above 0.2 for fracture (estimated from average opening of above 0.01 mm). Thus, as the specimen is gradually wetted from top to bottom, the wetting process in the matrix is dominated by the capillary force. In contrast, the wetting process in the fracture is governed by both capillary and gravitational effects.
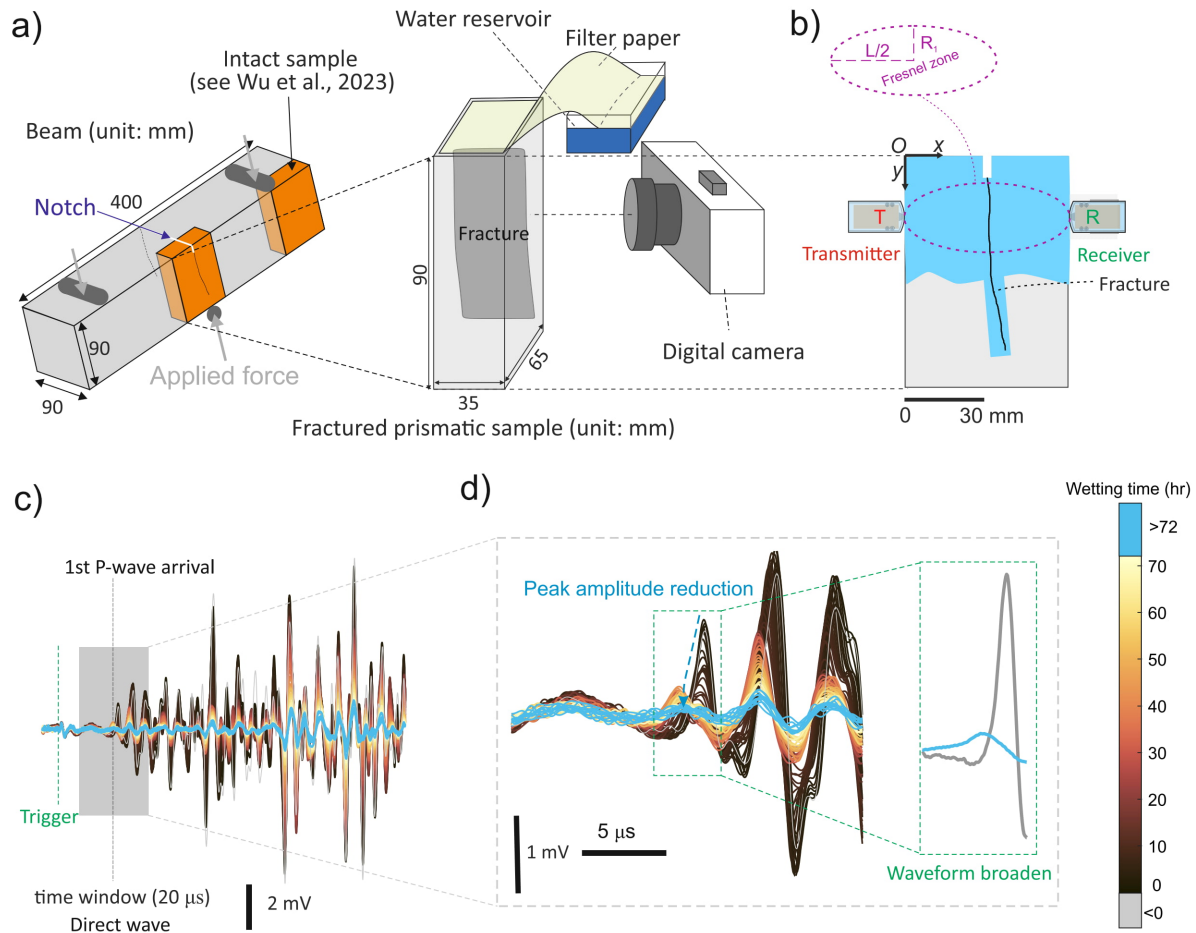
Figure 1. Schematic of the experimental setup. (a) A free-standing granite prism containing a fracture (gray curved plane) undergoing progressive wetting. (b) Acousto-mechanical monitoring using digital image correlation and ultrasonic pulse transmission. (c) Stacked waveforms received over a 16-hr drying stage followed by a 270-hr wetting stage. (d) Direct waves centered around the *P*-wave arrival within a time window of 20 μs.

2.3. Time-Lapse Acousto-Mechanical Monitoring

We utilize time-lapse digital image correlation (DIC) and ultrasound techniques to investigate the acousto-mechanical response of the fracture under gradual wetting. Monitoring methods are detailed in Text S2 in Supporting Information S1. Acoustic changes are measured using ultrasonic pulse transmission (Birch, 1960). In Figure 1b, a transmitter and a receiver (T-R) are installed on two sides of the specimen. This pair arrangement determines a Fresnel zone—a confocal prolate ellipsoidal region (dashed ellipse in Figure 1b) where direct waves mostly reveal elastic properties of this zone (Spetzler & Snieder, 2004). *P*-wave first ($n = 1$) Fresnel zone (P-FFZ) is adopted following the nomenclature in Wu, Selvadurai, Li, Sun, et al. (2023) with its minor axis R_1 given as:

$$R_1 = \frac{1}{2}\sqrt{\lambda L + \frac{\lambda^2}{4}}. \tag{1}$$

where λ is the wavelength and L is the T-R distance (65 mm). Ultrasonic pulses are emitted from the transmitter using a 200 V excitation voltage (P. A. Selvadurai et al., 2022; Wu et al., 2020, 2021). A survey is conducted every 15 min with 1,144 measurements obtained over 286 hr. In Figure 1c, waveforms acquired at 20 MHz are aligned at the trigger time (before: 4.7 μs, after: 97.7 μs). Direct waves are windowed within 20 μs (gray box) centered around the *P*-wave arrival in Figure 1d. The first peak amplitude is stable at around 1 mV before moisture uptake (gray), reduces significantly after 72 hr of the introduction of water (black to yellow), and eventually fades to the noise level (below 0.15 mV). The high-frequency content is dissipated during the moisture uptake as the waveform is observed to "broaden" (green inset). The ultrasonic data acquisition and processing,
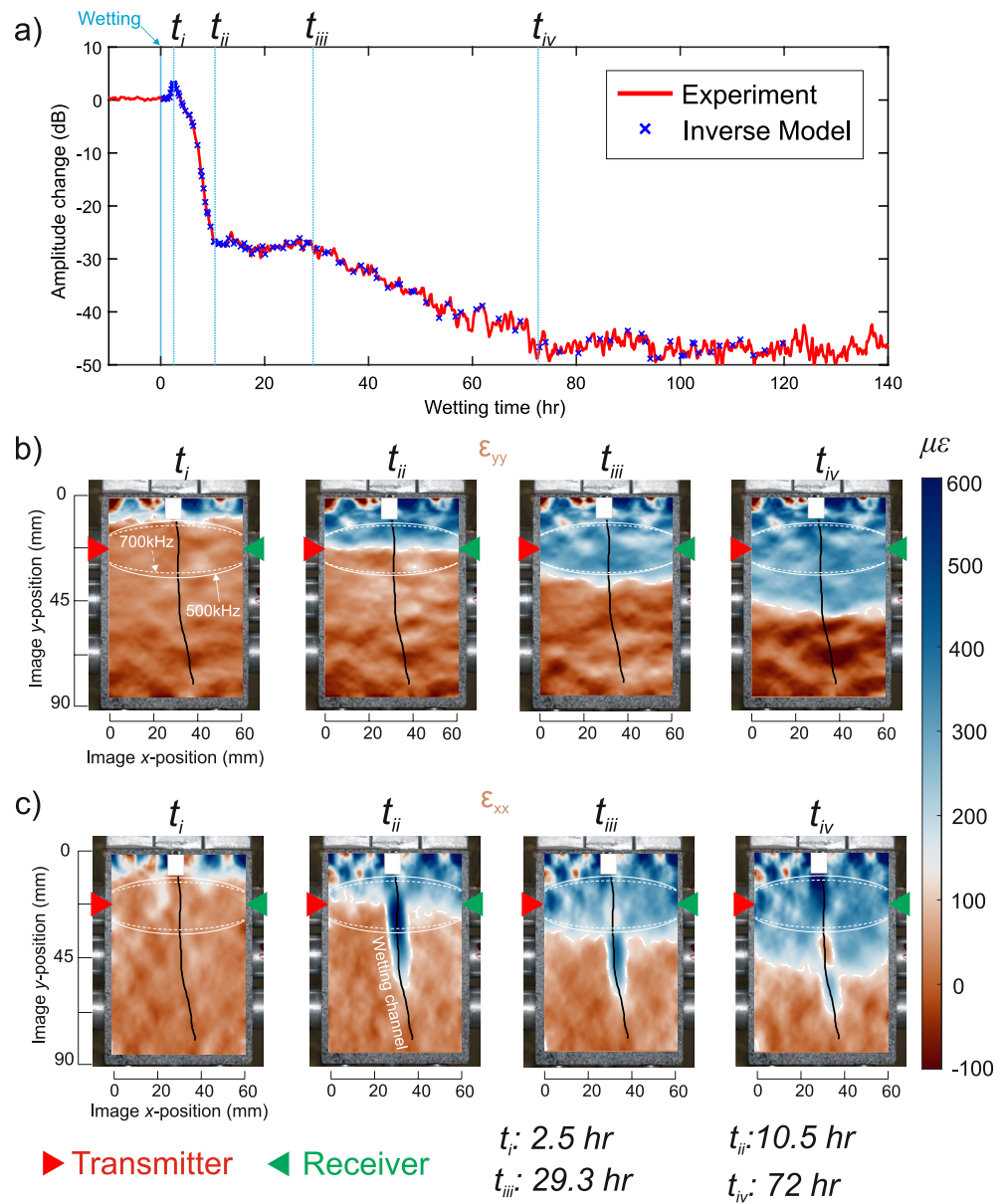
Figure 2. (a) Amplitude changes of direct waves in response to the wetting process, obtained from the experimental measurement (red solid line) and inverse modeling (blue crosses). Vertical blue lines indicate the main turning points of amplitude changes. (b) Vertical strain ϵ_{yy} and (c) horizontal strain ϵ_{xx} evolution on the frontal face of the specimen as the water is introduced. Black solid line denotes the location of the fracture.

including *P*-wave arrival picking, frequency bandwidth selection (500–700 kHz), and amplitude calculation, is detailed in Texts S2 and S3 in Supporting Information S1.

Besides ultrasonic monitoring, the frontal surface of the specimen is simultaneously imaged with a digital camera at 30-min intervals over 286 hr (Figure 1b). The acquired images are processed to calculate the strain field (Text S4 in Supporting Information S1) and track the wetting front movement (Text S5 in Supporting Information S1).

3. Results

Amplitude changes (ΔT_f) of the direct waves (Figure 1d) are analyzed over the entire experimental period, focusing on the gradual wetting phase. In Figure 2a, ΔT_f (red) is isolated over 150 hr (140 hr under progressive wetting). The beginning of the wetting phase (0 hr) is associated with introduction of the water to the top of the

specimen. Times corresponding to transitions in ΔT_f are marked as times i (2.5 hr), ii (10.5 hr), iii (29.3 hr), and iv (72 hr). The amplitude changes from inverse modeling (blue crosses) will be described later in Section 4.2.

To relate seismic attenuation (ΔT_f) to the wetting process and surface deformation of the specimen, vertical (ϵ_{yy}) and horizontal (ϵ_{xx}) strains are shown in Figures 2b and 2c, respectively. The full strain field on the frontal surface is shown for the times of interest in Figure 2a. The ϵ_{yy} evolution indicates the history of the moisture profile in the matrix, while the ϵ_{xx} evolution indicates the deformation history of the material surrounding the fracture. Strain contour at 100 $\mu\epsilon$ (white dashed line) is chosen to delineate (a) the movement of the wetting front in the host rock using ϵ_{yy} and (b) the fracture deformation using ϵ_{xx}. The ellipses show the size (minor axis R_1 of approximately 12.5 and 10 mm) of P-FFZ at 500 and 700 kHz. A white area (dimension: 9×7 mm) near the top surface is the notch used to create the fracture in the bending test, for which DIC results are not available. The black line around the central region indicates the fracture profile.

Prior to wetting, the specimen is equilibrated under ambient laboratory conditions with less than 0.15 dB variation of ΔT_f. After the water is introduced, the wetting front moves downward and enters into the P-FFZ of 500 kHz, and the fracture begins to open at time i with an observed increase in ΔT_f of 3 dB. A wetting channel, nearly symmetric around the fracture, is formed and migrates downward, for example, reaching a depth of about 55 mm and a width of about 8 mm at time ii. This channel is much ahead (by around 30 mm) of the wetting front in the matrix which reaches a depth of approximately 22.5 mm at time ii. The channel serves as a source for the surrounding matrix to imbibe due to the greater capillary forces in the microcracks which have a much smaller aperture than the macroscopic fracture. Consequently, a significant amount of horizontal strain is observed within the wetting channel with an average magnitude of 300–400 $\mu\epsilon$. There is a monotonic decrease in ΔT_f from 3 dB at time i to -26 dB at time ii.

After time ii, the wetting front migrates to the lower part of P-FFZ and leaves P-FFZ completely at time iii. ΔT_f remains stable at -26 ± 0.6 dB. As the wetting front continues to migrate downward and reaches the middle part (about $y = 48$ mm) at time iv, the wetting channel appears to stagnate at a depth of 65 mm. This may be because the fracture aperture decreases significantly, hindering moisture transportation. ϵ_{xx} within P-FFZ evolves significantly while ΔT_f decreases from -26 to -48 dB. After time iv, the direct waves are difficult to distinguish from the noise (see Figure 1d) until the end of the test. The ΔT_f evolution over the whole experimental period is provided in Figure S5 in Supporting Information S1.

4. Discussion

4.1. Effect of Progressive Wetting on Elastic Wave Transmission Across a Fracture

We analyze the influence of progressive wetting on the amplitude variations of the elastic waves transmitted across the fracture. We plot the amplitude variations (ΔT_f, originally in Figure 2a) in response to the vertical movement of the wetting front (detailed in Text S5 in Supporting Information S1) in Figure 3a. The vertical position of the T-R raypath is taken as the baseline. We also show the amplitude changes (ΔT_i, blue) of an intact specimen for comparison (Figure 1a). The purple area shows the differential region of the P-FFZ between 500 and 700 kHz.

Both ΔT_f and ΔT_i show some similarities in their responses. Amplitude changes are simultaneously amplified to a peak as the wetting front crosses the upper boundary of the P-FFZ at 500–700 kHz (time i). The similarity could be interpreted by the elastic wave reflection/refraction surrounding the P-FFZ in the bi-layered medium, where an interface between two layers is defined by the wetting front (Knott, 1899; Kovalyshen, 2018; Wu, Selvadurai, Li, Sun, et al., 2023; Zoeppritz, 1919). In Figure 3b, the incident P waves arrive at the wetting front at time i, and are converted into refracted P (denoted as Pp) and S (denoted as Ps) waves. Since the wetted part has a higher acoustic impedance ($Z_p = 1.21 \times 10^7$ Pa $\cdot$ s/m^3) compared to the dry part ($Z_p = 1.08 \times 10^7$ Pa $\cdot$ s/m^3), the refracted waves remain in phase with the direct P-waves propagating along the T-R path and contribute to the synthesized waveform. This explains the amplification observed in ΔT_f and ΔT_i at time i. When the wetting front arrives at the position of the T-R raypath at time ii, there is a phase shift of 180° between the refracted and direct P-waves. This explains the monotonic decrease of ΔT_f and ΔT_i from time i to ii.

However, the three notable deviations between ΔT_f and ΔT_i indicate the effect of the fracture. Before time ii, ΔT_i exhibits more prominent variations compared with ΔT_f. This occurs because the refracted waves at the wetting front undergo seismic attenuation while traveling across the fracture. If these attenuated refracted waves are in or out of phase with the direct P-waves, ΔT_f will show less variation.
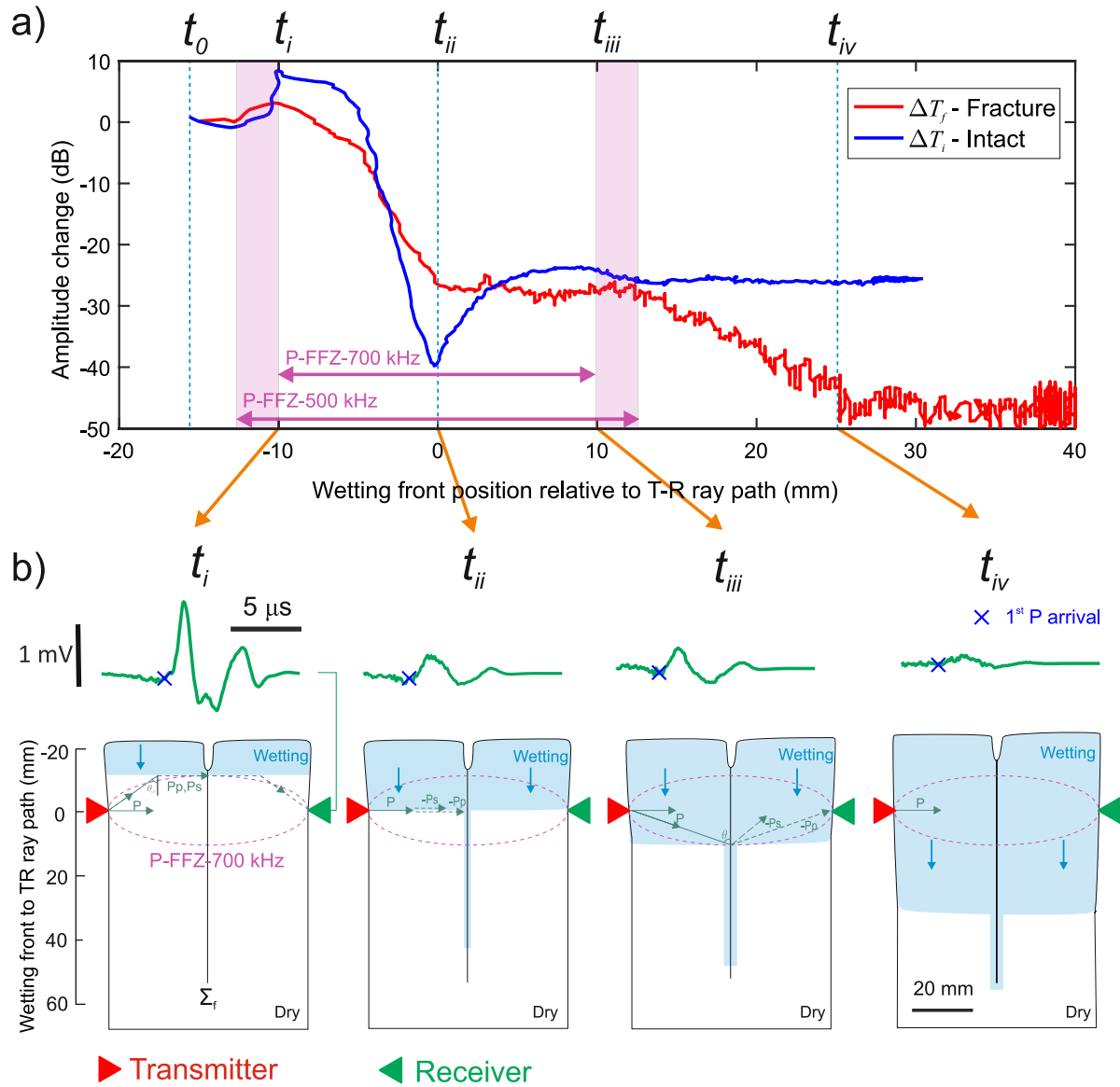
Figure 3. (a) Amplitude changes in the fractured (red) specimens, compared with the intact (blue) specimen (Wu, Selvadurai, Li, Sun, et al., 2023), in response to the wetting front migration. (b) Top: Representative waveforms. Bottom: Schematic illustration of elastic wave interaction with the fracture associated with a migrating wetting front.

After time ii, the refracted waves remain out of phase with the direct P-waves but their amplitudes decrease to the incident angle as the wetting front progresses. Consequently, when refracted waves are synthesized with direct P-waves in the intact rock, a partial recovery of ΔT_i is observed. In contrast, ΔT_f shows little variation. We propose that the enhanced seismic attenuation across the progressively wetted fracture offsets the recovery in the intact rock.

After time iii, ΔT_i generally plateaus as the elastic properties within the P-FFZ become more homogeneous. However, ΔT_f decreases significantly until it becomes indistinguishable from the noise. This indicates that the fracture remains an active role, making it difficult for the elastic waves to transmit.

4.2. How Does Fracture Stiffness Vary Due To Gradual Wetting?

The fracture can be modeled as a non-welded interface, characterized by contact asperities and adjacent voids (Johnson, 1985; Persson, 2006; Tsang & Witherspoon, 1981). Across the fracture, stress remains continuous, but displacement is discontinuous (Cook, 1992; Pyrak-Nolte et al., 1990; Schoenberg, 1980). For P-waves incident

normal to the fracture, the ratio of normal stress to displacement discontinuity across the fracture gives the specific normal stiffness, κ_n. The magnitude of the transmission coefficient, $|T(\omega)|$, responds to κ_n:

$$|T(\omega)| = \frac{1}{1 + \hat{\omega}^2} = \frac{1}{1 + \left(\frac{\omega Z_p}{2\kappa_n}\right)^2} \tag{2}$$

where ω and $\hat{\omega}$ are the angular frequency and dimensionless angular frequency, respectively. As κ_n approaches infinity, $|T(\omega)|$ becomes unity, indicative of the absence of a fracture. For our analysis, $|T(\omega)|$ of the intact dry specimen is set to unity. For the fractured specimen, despite small deflection (less than 2°), we assume the fracture to be vertically planar, allowing the application of Equation 2. Following these assumptions, we measure $|T(\omega)|$ as 0.2 and calculate κ_n^{dry} as 4,320 GPa/m for the dry fracture (orange circle in Figure 4a). Measurements and calculations of κ_n^{dry} are detailed in Text S6 in Supporting Information S1. If κ_n decreases while Z_p and ω maintain, $|T(\omega)|$ will decrease. According to Pyrak-Nolte et al. (1990), there is no effect of viscous coupling from the water on $|T(\omega)|$ of incident P-waves normal to the fracture.

We decipher the evolution of the fracture stiffness, κ_n^{wet}, as the fractured rock undergoes progressive wetting. By directly inserting ΔT_f into Equation 2, we observe that κ_n^{wet} (black dotted line in Figure 4b) decreases completely by over two orders of magnitude since the water reaches the top end of the fracture ($Y_f = 0$). Y_f denotes the wetted depth of the fracture. Derived κ_n^{wet} may be subject to some bias, as the refraction of elastic waves at the migrating wetting front could affect ΔT_f.

We further develop an inverse model with parameters constrained by experimental data. A 2D finite element model, simulating elastic wave propagation in a bi-layered fractured medium, is constructed in Figure S7 in Supporting Information S1. The fracture is represented by a non-welded interface assuming uniform stiffness. The wetting front, which we assume to be flat and sharply defined, is modeled as a welded interface (Knott, 1899; Kovalyshen, 2018; Wu, Selvadurai, Li, Sun, et al., 2023; Zoeppritz, 1919) with the parameters constrained by the water imbibition test of the fractured specimen. The fracture stiffness is calibrated by minimizing the discrepancy in amplitude changes between numerical and experimental waveforms (see their close match in Figure 2a). The modeling methodology is detailed in Text S7 in Supporting Information S1.

In Figure 4b, the back-calculated stiffness κ_n^{wet} (orange solid line) evolves from $\kappa_n^{dry} = 4,320$ GPa/m at time i and exponentially decays as the wetting front progressively migrates downwards. The difference in κ_n^{wet} between inverse modeling and experiment up to time iii indicates the effect of wetting front movement on the elastic wave transmission across the fracture. The Pearson correlation coefficient between $\ln\kappa_n^{wet}$ (inverse modeling) and Y_f is 0.98 at 95% confidence level, indicating a strong correlation. An empirical relationship between κ_n^{wet} and Y_f is obtained as:

$$\kappa_n^{wet} = \kappa_n^{dry} \times e^{-a \times Y_f} \tag{3}$$

and shown as blue dashed line in Figure 4b. a is a constant, taking 0.1444 for our specimen.

Once the wetting front completely passes the P-FFZ (time iii), no elastic wave reflection/refraction occurs at the wetting front. Consequently, the wetting front will no longer affect the amplitude; thus, κ_n^{wet} from the inverse modeling (orange solid line) and experiment (black dotted line) are observed to agree well (Figure 4b) which will be further discussed in Section 4.3. After time iv, the waveforms are completely immersed in the background noise (Figure S1b in Supporting Information S1), and κ_n^{wet} eventually stabilizes at around 17 ± 2 GPa/m (Figure 4b). The implementation of such an inverse modeling methodology allows us to better determine the moisture-dependent fracture stiffness.

4.3. Why Does Fracture Stiffness Decrease as the Wetting Front Migrates Along the Fracture?

The exponential decay of fracture stiffness with the wetting front migration (Figure 4b and Equation 3) highlights inherent relationships among the water imbibition, mechanical deformation, and seismic attenuation of a single wetted fracture (Figure 4c). Along the rough interfaces, there is a sparse set of dilute contacts at different length scales (Persson, 2006). During water imbibition, the adsorption of water molecules onto the contact patches at asperities leads to a reduction in the free surface energy of the asperity minerals, followed by a volumetric expansion at the asperities (Dobrzanski et al., 2021). This causes an increased separation distance between the opposing walls and a decreased real contact area. As a result, the mechanical interactions at these asperities become less
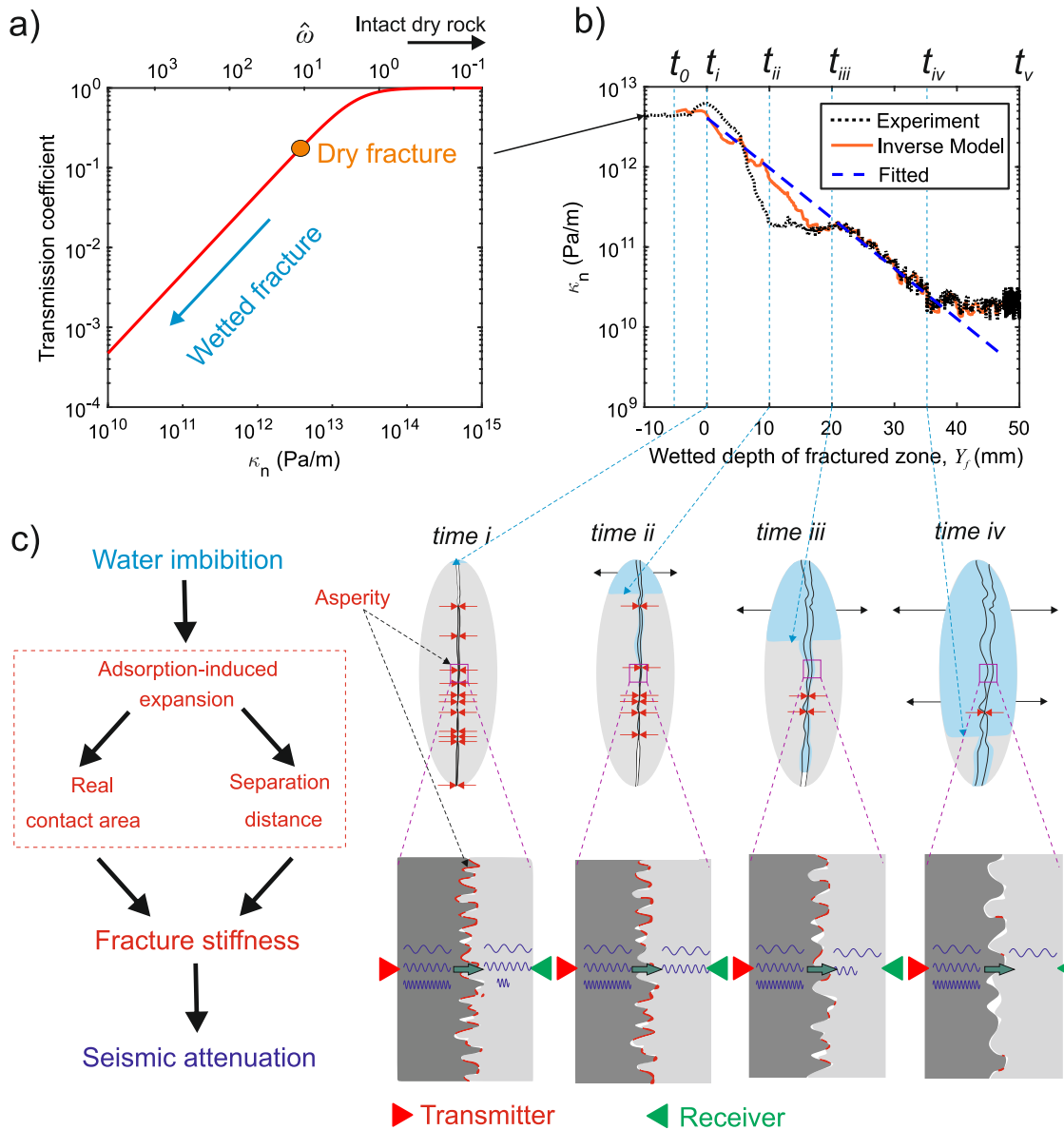
Figure 4. (a) Variations of the transmission coefficient for incident *P*-waves normal to the fracture as a function of the fracture specific normal stiffness, κ_n. (b) Evolution of fracture stiffness subject to gradual wetting derived from inverse modeling (orange) and direct ultrasonic measurements (black). (c) Schematic showing the inherent relationships between the water imbibition, mechanical deformation, and seismic attenuation of a single wetted fracture.

intense (analogous to a release of contact force) and the total number of asperities in contact decreases. At the macroscopic level, as the wetting front progresses along the fracture, the opposing rough walls tend to separate, decreasing the fracture stiffness. When elastic waves impinge almost normally on the fracture and transmit through the reduced contact area, more high-frequency, short-wavelength elastic waves are reflected where some low-frequency, long-wavelength portions can still pass through.

At ultrasonic frequencies, elastic waves through wetted microcracks can generate local pressure gradients, resulting in fluid flow and viscous dissipation (Müller et al., 2010). This wave-induced flow could lead to decreased fracture stiffness and wave transmission. Imbibed water may also aid the contact by volumetrically filling the fracture voids, thereby promoting transmission, as observed for saturated fractures under compression (Pyrak-Nolte et al., 1990). These processes however are expected to have minor effects on our results.

In this work, we have experimentally derived a formulation to describe the seismo-hydro-mechanical behavior of wetted single fractures under tension, which opens the door to use seismic waves for characterizing fracture

geometry and tracking water infiltration along fractures, which play an essential role in unsaturated flow in near-surface bedrocks (Pruess, 1999). This could help us better understand and predict landslide behavior that is strongly affected by seasonal rainwater infiltration into basal shear zones (Finnegan et al., 2021, 2022). Useful insights can also be yielded into the spatiotemporal evolution of fracture stiffness in unsaturated bedrocks, which may play an important role in groundwater recharge-induced reversible ground surface displacements (Oestreicher et al., 2023) and landslide motion driven by moisture changes (Whiteley et al., 2019). The experimentally derived formulation in our study can be combined with the discrete fracture network modeling approach (Lei & Sornette, 2021a, 2021b) and seismic attenuation modeling in unsaturated fractures (Solazzi et al., 2020) to unravel and predict the seismo-hydro-mechanical behavior of complex fracture systems subject to water infiltration in near-surface environments. We will explore these topics in our future work.

5. Conclusions

Based on well-controlled laboratory experiments, we investigated the relationships among water imbibition, mechanical deformation, and seismic attenuation in single fractures subjected to tension and progressive wetting. We found that wave transmission strongly correlates with the wetting front movement of infiltrated water along the fracture where significant attenuation occurs since adsorption-induced expansion at asperities reduces the real contact area and the number of contact patches. As a result, less seismic energy can be transmitted across the fracture whose stiffness undergoes moisture-dependent weakening. Using an inverse modeling approach, we found the fracture stiffness follows an exponential decrease over about two orders of magnitude with the wetting front position as it moves along the fracture. Our results, elucidating the strong control of water infiltration on seismic wave propagation in fractured rocks, have important implications for many geophysical and geoengineering applications.

Data Availability Statement

Data analyzed in this study is available on the ETH Research Collection and can be downloaded from Wu, Selvadurai, Li, Kerry, et al. (2023).

References

Archard, J. F. (1957). Elastic deformation and the laws of friction. *Proceedings of the Royal Society of London. Series A. Mathematical and Physical Sciences*, *243*(1233), 190–205. https://doi.org/10.1098/rspa.1957.0214

Baud, P., Zhu, W., & Wong, T.-f. (2000). Failure mode and weakening effect of water on sandstone. *Journal of Geophysical Research*, *105*(B7), 16371–16389. https://doi.org/10.1029/2000JB900087

Birch, F. (1960). The velocity of compressional waves in rocks to 10 kilobars: 1. *Journal of Geophysical Research*, *65*(4), 1083–1102. https://doi.org/10.1029/jz065i004p01083

Bowden, F. P., & Tabor, D. (2001). *The friction and lubrication of solids* (Vol. 1). Oxford university press.

Burjánek, J., Gischig, V., Moore, J. R., & Fäh, D. (2017). Ambient vibration characterization and monitoring of a rock slope close to collapse. *Geophysical Journal International*, *212*(1), 297–310. https://doi.org/10.1093/gji/ggx424

Choi, M.-K., Bobet, A., & Pyrak-Nolte, L. J. (2014). The effect of surface roughness and mixed-mode loading on the stiffness ratio $\kappa x/\kappa z$ for fractures. *Geophysics*, *79*(5), D319–D331. https://doi.org/10.1190/geo2013-0438.1

Chugh, Y. P., & Missavage, R. A. (1981). Effects of moisture on strata control in coal mines. *Trans Am Inst Min Metall Pet Eng Soc Min Eng Aime, V*, *270*(4), 1816–1820. https://doi.org/10.1016/0148-9062(82)91765-x

Cook, N. G. (1992). Natural joints in rock: Mechanical, hydraulic and seismic behaviour and properties under normal stress. In *International journal of rock mechanics and mining sciences & geomechanics abstracts* (Vol. 29, No. (3), pp. 198–223). https://doi.org/10.1016/0148-9062(92)93656-5

David, C., Barnes, C., Desrues, M., Pimienta, L., Sarout, J., & Dautriat, J. (2017). Ultrasonic monitoring of spontaneous imbibition experiments: Acoustic signature of fluid migration. *Journal of Geophysical Research: Solid Earth*, *122*(7), 4931–4947. https://doi.org/10.1002/2016JB013804

David, C., Sarout, J., Dautriat, J., Pimienta, L., Michée, M., Desrues, M., & Barnes, C. (2017). Ultrasonic monitoring of spontaneous imbibition experiments: Precursory moisture diffusion effects ahead of water front. *Journal of Geophysical Research: Solid Earth*, *122*(7), 4948–4962. https://doi.org/10.1002/2017JB014193

Diederichs, M. S. (2007). The 2003 Canadian geotechnical colloquium: Mechanistic interpretation and practical application of damage and spalling prediction criteria for deep tunnelling. *Canadian Geotechnical Journal*, *44*(9), 1082–1116. https://doi.org/10.1139/T07-033

Dieterich, J. H., & Kilgore, B. D. (1994). Direct observation of frictional contacts: New insights for state-dependent properties. *Pure and Applied Geophysics*, *143*(1–3), 283–302. https://doi.org/10.1007/bf00874332

Dobrzanski, C. D., Gurevich, B., & Gor, G. Y. (2021). Elastic properties of confined fluids from molecular modeling to ultrasonic experiments on porous solids. *Applied Physics Reviews*, *8*(2), 21317. https://doi.org/10.1063/5.0024114

Finnegan, N. J., Brodsky, E. E., Savage, H. M., Nereson, A. L., & Murphy, C. R. (2022). Seasonal slow landslide displacement is accommodated by mm-scale stick-slip events. *Geophysical Research Letters*, *49*(20), e2022GL099548. https://doi.org/10.1029/2022GL099548

Finnegan, N. J., Perkins, J. P., Nereson, A. L., & Handwerger, A. L. (2021). Unsaturated flow processes and the onset of seasonal deformation in slow-moving landslides. *Journal of Geophysical Research: Earth Surface*, *126*(5), e2020JF005758. https://doi.org/10.1029/2020JF005758

Geimer, P. R., Finnegan, R., & Moore, J. R. (2020). Sparse ambient resonance measurements reveal dynamic properties of freestanding rock arches. *Geophysical Research Letters*, *47*(9), e2020GL087239. https://doi.org/10.1029/2020GL087239

Gheibi, A., & Hedayat, A. (2018). Ultrasonic investigation of granular materials subjected to compression and crushing. *Ultrasonics*, *87*, 112–125. https://doi.org/10.1016/j.ultras.2018.02.006

Greenwood, J. A., & Williamson, J. B. P. (1966). Contact of nominally flat surfaces. *Proceedings of the Royal Society of London. Series A. Mathematical and Physical Sciences*, *295*(1442), 300–319. https://doi.org/10.1098/rspa.1966.0242

Johnson, K. L. (1985). *Contact mechanics*. Cambridge University Press. https://doi.org/10.1017/CBO9781139171731

Kame, N., Nagata, K., Nakatani, M., & Kusakabe, T. (2014). Feasibility of acoustic monitoring of strength drop precursory to earthquake occurrence. *Earth, Planets and Space*, *66*(1), 41. https://doi.org/10.1186/1880-5981-66-41

Kaproth, B. M., & Marone, C. (2013). Slow earthquakes, preseismic velocity changes, and the origin of slow frictional stick-slip. *Science*, *341*(6151), 1229–1232. https://doi.org/10.1126/science.1239577

Kendall, K., & Tabor, D. (1971). An ultrasonic study of the area of contact between stationary and sliding surfaces. *Proceedings of the Royal Society of London. A. Mathematical and Physical Sciences*, *323*(1554), 321–340. https://doi.org/10.1098/rspa.1971.0108

Knott, C. G. (1899). Reflexion and refraction of elastic waves, with seismological applications. *The London, Edinburgh, and Dublin Philosophical Magazine and Journal of Science*, *48*(290), 64–97. https://doi.org/10.1080/14786449908621305

Kovalyshen, Y. (2018). Comment on "ultrasonic monitoring of spontaneous imbibition experiments: Precursory moisture diffusion effects ahead of water front" by David et al. (2017). *Journal of Geophysical Research: Solid Earth*, *123*(8), 6607–6609. https://doi.org/10.1029/2018JB016040

Lei, Q., & Sornette, D. (2021a). Anderson localisation and reentrant delocalisation of tensorial elastic waves in two-dimensional fractured media. *Europhysics Letters*, *136*(3), 39001. https://doi.org/10.1209/0295-5075/ac225d

Lei, Q., & Sornette, D. (2021b). Transport and localization of elastic waves in two-dimensional fractured media: Consequences on scattering attenuation. *Journal of Geophysical Research: Solid Earth*, *126*(6), e2020JB021178. https://doi.org/10.1029/2020JB021178

Li, Y., Leith, K., Perras, M. A., & Loew, S. (2021). Digital image correlation–based analysis of hygroscopic expansion in Herrnholz granite. *International Journal of Rock Mechanics and Mining Sciences*, *146*, 104859. https://doi.org/10.1016/j.ijrmms.2021.104859

Li, Y., Leith, K., Perras, M. A., & Loew, S. (2022). Effect of ambient humidity on the elasticity and deformation of unweathered granite. *Journal of Geophysical Research: Solid Earth*, *127*(11), e2022JB024004. https://doi.org/10.1029/2022JB024004

Müller, T. M., Gurevich, B., & Lebedev, M. (2010). Seismic wave attenuation and dispersion resulting from wave-induced flow in porous rocks - A review. *Geophysics*, *75*(5), 75A147–75A164. https://doi.org/10.1190/1.3463417

Nagata, K., Nakatani, M., & Yoshida, S. (2008). Monitoring frictional strength with acoustic wave transmission. *Geophysical Research Letters*, *35*(6), L06310. https://doi.org/10.1029/2007GL033146

Oestreicher, N., Lei, Q., Loew, S., & Roques, C. (2023). Bedrock fractures control groundwater-driven mountain slope deformations. *Journal of Geophysical Research: Earth Surface*, *128*(11), e2022JF006885. https://doi.org/10.1029/2022JF006885

Persson, B. N. (2006). Contact mechanics for randomly rough surfaces. *Surface Science Reports*, *61*(4), 201–227. https://doi.org/10.1016/J.SURFREP.2006.04.001

Pruess, K. (1999). A mechanistic model for water seepage through thick unsaturated zones in fractured rocks of low matrix permeability. *Water Resources Research*, *35*(4), 1039–1051. https://doi.org/10.1029/1998wr900100

Pyrak-Nolte, L. J., Myer, L. R., & Cook, N. G. (1990). Transmission of seismic waves across single natural fractures. *Journal of Geophysical Research*, *95*(B6), 8617–8638. https://doi.org/10.1029/JB095iB06p08617

Schoenberg, M. (1980). Elastic wave behavior across linear slip interfaces. *The Journal of the Acoustical Society of America*, *68*(5), 1516–1521. https://doi.org/10.1121/1.385077

Scuderi, M. M., Marone, C., Tinti, E., Di Stefano, G., & Collettini, C. (2016). Precursory changes in seismic velocity for the spectrum of earthquake failure modes. *Nature Geoscience*, *9*(9), 695–700. https://doi.org/10.1038/ngeo2775

Selvadurai, A. P. S., Letendre, A., & Hekimi, B. (2011). Axial flow hydraulic pulse testing of an argillaceous limestone. *Environmental Earth Sciences*, *64*(8), 2047–2058. https://doi.org/10.1007/s12665-011-1027-7

Selvadurai, P. A., Wu, R., Bianchi, P., Niu, Z., Michail, S., Madonna, C., & Wiemer, S. (2022). A methodology for reconstructing source properties of a conical piezoelectric actuator using array-based methods. *Journal of Nondestructive Evaluation*, *41*(1), 23. https://doi.org/10.1007/s10921-022-00853-6

Shokouhi, P., Jin, J., Wood, C., Rivière, J., Madara, B., Elsworth, D., & Marone, C. (2020). Dynamic stressing of naturally fractured rocks: On the relation between transient changes in permeability and elastic wave velocity. *Geophysical Research Letters*, *47*(1), e2019GL083557. https://doi.org/10.1029/2019GL083557

Shreedharan, S., Bolton, D. C., Rivière, J., & Marone, C. (2020). Preseismic Fault creep and elastic wave amplitude precursors scale with lab earthquake magnitude for the continuum of tectonic failure modes. *Geophysical Research Letters*, *47*(8), e2020GL086986. https://doi.org/10.1029/2020GL086986

Shreedharan, S., Bolton, D. C., Rivière, J., & Marone, C. (2021). Competition between preslip and deviatoric stress modulates precursors for laboratory earthquakes. *Earth and Planetary Science Letters*, *553*, 116623. https://doi.org/10.1016/J.EPSL.2020.116623

Solazzi, S. G., Hunziker, J., Caspari, E., Rubino, J. G., Favino, M., & Holliger, K. (2020). Seismic signatures of fractured porous rocks: The partially saturated case. *Journal of Geophysical Research: Solid Earth*, *125*(8), e2020JB019960. https://doi.org/10.1029/2020JB019960

Spetzler, J., & Snieder, R. (2004). The Fresnel volume and transmitted waves. *Geophysics*, *69*(3), 653–663. https://doi.org/10.1190/1.1759451

Su, G. W., Geller, J. T., Pruess, K., & Wen, F. (1999). Experimental studies of water seepage and intermittent flow in unsaturated, rough-walled fractures. *Water Resources Research*, *35*(4), 1019–1037. https://doi.org/10.1029/1998wr900127

Tinti, E., Scuderi, M. M., Scognamiglio, L., Di Stefano, G., Marone, C., & Collettini, C. (2016). On the evolution of elastic properties during laboratory stick-slip experiments spanning the transition from slow slip to dynamic rupture. *Journal of Geophysical Research: Solid Earth*, *121*(12), 8569–8594. https://doi.org/10.1002/2016JB013545

Tsang, Y. W., & Witherspoon, P. A. (1981). Hydromechanical behavior of a deformable rock fracture subject to normal stress. *Journal of Geophysical Research*, *86*(B10), 9287–9298. https://doi.org/10.1029/JB086iB10p09287

Weber, S., Fäh, D., Beutel, J., Faillettaz, J., Gruber, S., & Vieli, A. (2018). Ambient seismic vibrations in steep bedrock permafrost used to infer variations of ice-fill in fractures. *Earth and Planetary Science Letters*, *501*, 119–127. https://doi.org/10.1016/J.EPSL.2018.08.042

Whiteley, J. S., Chambers, J. E., Uhlemann, S., Wilkinson, P. B., & Kendall, J. M. (2019). Geophysical monitoring of moisture-induced landslides: A review. *Reviews of Geophysics*, *57*(1), 106–145. https://doi.org/10.1029/2018RG000603

Wu, R., Selvadurai, P. A., Chen, C., & Moradian, O. (2021). Revisiting piezoelectric sensor calibration methods using elastodynamic body waves. *Journal of Nondestructive Evaluation*, *40*(3), 68. https://doi.org/10.1007/s10921-021-00799-1

Wu, R., Selvadurai, P. A., Chen, C. J., & Moradian, O. (2020). A FEM-based methodology to acquire broadband empirical Green's functions to understand characterization tests of acoustic emission sensors. In *54th U.S. rock mechanics/geomechanics symposium*.

Wu, R., Selvadurai, P. A., Li, Y., Kerry, L., Lei, Q., & Loew, S. (2023). Data for laboratory acousto-mechanical study into moisture-induced reduction of fracture stiffness in granite [Dataset]. ETH Zurich. https://doi.org/10.3929/ethz-b-000582539

Wu, R., Selvadurai, P. A., Li, Y., Sun, Y., Leith, K., & Loew, S. (2023). Laboratory acousto-mechanical study into moisture-induced changes of elastic properties in intact granite. *International Journal of Rock Mechanics and Mining Sciences*, *170*, 105511. https://doi.org/10.1016/j.ijrmms.2023.105511

Zoeppritz, K. (1919). On the reflection and propagation of seismic waves. *Gottinger Nachrichten*, *1*(5), 66–84.

References From the Supporting Information

Akaike, H. (1974). A new look at the statistical model identification. *IEEE Transactions on Automatic Control*, *19*(6), 716–723. https://doi.org/10.1109/TAC.1974.1100705

ASTM D-18. (2008). Standard test method for laboratory determination of pulse velocities and ultrasonic elastic constants of rock. In *Annual book of ASTM standards* (pp. 356–363). ASTM International.

Aydin, A. (2015). Upgraded ISRM suggested method for determining sound velocity by ultrasonic pulse transmission technique. In *The ISRM suggested methods for rock characterization, testing and monitoring* (pp. 95–99). Springer International Publishing.

Blaber, J., Adair, B., & Antoniou, A. (2015). Ncorr: Open-Source 2D digital image correlation Matlab software. *Experimental Mechanics*, *55*(6), 1105–1122. https://doi.org/10.1007/s11340-015-0009-1

Bracewell, R. N. (1986). *The Fourier transform and its applications* (Vol. 31999). McGraw-Hill.

Eitzen, D. G., & Wadley, H. N. G. (1984). Acoustic emission: Establishing the fundamentals. *Journal of research of the National Bureau of Standards*, *89*(1), 75–100. https://doi.org/10.6028/jres.089.008

Glaser, S. D., Weiss, G. G., & Johnson, L. R. (1998). Body waves recorded inside an elastic half-space by an embedded, wideband velocity sensor. *The Journal of the Acoustical Society of America*, *104*(3), 1404–1412. https://doi.org/10.1121/1.424350

Johnston, D. H., Toksöz, M. N., & Timur, A. (1979). Attenuation of seismic waves in dry and saturated rocks: II. Mechanisms. *Geophysics*, *44*(4), 691–711. https://doi.org/10.1190/1.1440970

Kurz, J. H., Grosse, C. U., & Reinhardt, H. W. (2005). Strategies for reliable automatic onset time picking of acoustic emissions and of ultrasound signals in concrete. *Ultrasonics*, *43*(7), 538–546. https://doi.org/10.1016/J.ULTRAS.2004.12.005

Molyneux, J. B., & Schmitt, D. R. (1999). First-break timing: Arrival onset times by direct correlation. *Geophysics*, *64*(5), 1492–1501. https://doi.org/10.1190/1.1444653

Peraldi, R., & Clement, A. (1972). Digital processing of refraction data study of first arrivals. *Geophysical Prospecting*, *20*(3), 529–548. https://doi.org/10.1111/j.1365-2478.1972.tb00653.x

Toksöz, M. N., Johnston, D. H., & Timur, A. (1979). Attenuation of seismic waves in dry and saturated rocks: I. Laboratory measurements. *Geophysics*, *44*(4), 681–690. https://doi.org/10.1190/1.1440969

Winkler, K., & Nur, A. (1979). Pore fluids and seismic attenuation in rocks. *Geophysical Research Letters*, *6*(1), 1–4. https://doi.org/10.1029/GL006i001p00001